Coupling Coefficient Analysis and Experimental Evaluation of Dynamic Wireless Power Transfer for Battery-Electric Locomotives

Xiuhu Sun, *Graduate Student Member, IEEE*, Xiwen Xu, *Member, IEEE*, Karl Lin, Shen-En Chen, Tiefu Zhao, *Senior Member, IEEE*

***Abstract*—Wireless power transfer (WPT) offers a promising solution for continuous and contactless energy delivery to battery-electric locomotives (BELs). It enables in-motion charging, which can significantly reduce the need for prolonged static charging sessions and allow for smaller onboard battery capacities. This paper presents a dynamic wireless power transfer (DWPT) system specifically designed for BEL applications, employing a parallel synchronized multiple LCL-S compensation topology operating at a switching frequency of 85 kHz. A method for calculating the dynamic coupling coefficient k is proposed to model the time-varying magnetic coupling during motion. To validate the system, a prototype incorporating three transmitters (Txs), one receiver (Rx), and a W-I-shaped magnetic coupler is developed and tested. During static charging, the experimental results demonstrate a peak DC-DC efficiency of 94.73% at 3.1 kW input power, with over 92% efficiency sustained across a wide range of input voltages and output load resistances. During dynamic charging, the system maintains a stable efficiency with the maximum value of approximately 89%. These results also show agreement with theoretical predictions, validating the system's performance and robustness.**

***Index Terms*—Wireless power transfer (WPT), inductive power transfer (IPT), dynamic wireless power transfer (DWPT), coupling coefficient, finite element (FE) analysis.**

I. Introduction

ELECTRIC locomotives, compared with diesel trains, offer superior energy efficiency and produce zero direct emissions in the transportation sector. Their enhanced environmental performance aligns with the principles of sustainable development, making them a favorable choice for future railway systems. Consequently, electric locomotives are being increasingly adopted worldwide [1]. On the other hand, there are still many areas that continue to operate numerous inefficient, pollution-intensive diesel locomotives. The transition to electric railways is pivotal for environmental sustainability. However, the substantial associated high upfront capital costs in infrastructure and electric locomotives pose a considerable barrier [2]. In the United States, for instance, the cost of electrifying the railway by overhead catenary system (OCS) can range from $3 million to $30 million per track kilometer [3], [4], and a new electric locomotive might cost $2.7 million to $10 million [5]–[7]. As a result, less than 1% of its railway is electrified, despite having the largest railway network in the world [8].

Converting diesel locomotives into battery-electric locomotives (BELs) by equipping them with battery systems and charging them using dedicated infrastructure is a feasible solution for railway electrification [9], [10]. Compared with constructing OCS, this approach requires only the installation of charging facilities without the need to reconstruct the entire railway network. Meanwhile, it enables the reuse of existing diesel locomotives through electrification, rather than purchasing new rolling stock, thereby significantly reducing investment [11]. Moreover, compared to conventional diesel locomotives, the total cost of ownership (TCO) of converted BELs is substantially lower, only 67.65% of the diesel locomotives over a 20-year operational period [11].

The BEL solution involves stationary wired charging setups complicated by logistical challenges and restricted by environmental conditions. It requires handling bulky, high-voltage cables, which can be labor-intensive and pose safety risks. In addition, due to the current low battery power density, the battery pack must have a large volume and a heavy weight to meet the huge energy needs of locomotive operation. For instance, a BEL weighing 196 tons and powered by an 8.5 MWh battery pack could require 42.5 to 60.7 tons of lithium nickel manganese cobalt oxide (NMC) batteries, assuming an energy density of 140–200 Wh/kg [12]. This battery mass would account for approximately 21.7% to 31.0% of the total vehicle weight. The excessive weight significantly increases the cost and reduces operational efficiency.

To address these limitations, wireless power transfer (WPT), particularly inductive power transfer (IPT), has emerged as a promising alternative for BEL charging [13]–[16]. In addition to its technical advantages, WPT eliminates the need for cumbersome cables, thereby reducing manual labor and improving operational safety. More importantly, it facilitates dynamic charging during vehicle operation, substantially reducing charging time and allowing for smaller battery packs [17]. These advantages collectively contribute to cost

This work was supported by the U.S. Department of Transportation Federal Railroad Administration (FRA) under project 693JJ621C000002.

Portions of the research were presented at the 2024 IEEE Transportation Electrification Conference (ITEC) in Chicago, Illinois, under the title "Static and Dynamic Analysis of Wireless Power Transfer for Battery Electric Locomotives".

Xiuhu Sun, Xiwen Xu, and Tiefu Zhao (corresponding author) are with the Electrical and Computer Engineering Department, University of North Carolina at Charlotte, Charlotte, NC 28223, USA (e-mail: xsun17@charlotte.edu, xxu12@alumni.uncc.edu, Tiefu.Zhao@charlotte.edu).

Karl Lin and Shen-En Chen are with the Civil and Environmental Engineering Department, University of North Carolina at Charlotte, Charlotte, NC 28223, USA (e-mail: klin5@charlotte.edu, schen12@charlotte.edu).

reduction, efficiency improvement, and enhanced practicality. In the EV sector, WPT standards are evolving to ensure interoperability, alignment, and safety. Key standards include SAE J2954 for light-duty plug-in EVs [18], SAE J2954/2 for heavy-duty EVs [19], and the upcoming SAE J2954/3 for dynamic charging. Other standards, including the IEC 61980 series and ISO 5474-4 [20], provide international guidance for stationary and dynamic WPT. While specific standards for railway WPT remain under development, research in this area has grown steadily over the past decade. Table I summarizes selected WPT systems for railway applications since 2010, listing active research institutions and key system parameters. The transmitted power in these studies ranges from a few kilowatts up to several megawatts, with static power transfer efficiencies varying from 74% to 94%.

Within these studies, Xu et al. develop a railway WPT system featuring a discrete W-I-shaped core design and an LCL-S compensation topology [35], [36], which achieves a relatively high coupling coefficient (k) while significantly reducing the amount of magnetic material required. Compared to other designs, this approach reduces magnetic material usage by up to 93.2%, with only a 31.6% decrease in the coupling coefficient. Initial tests show a static DC-DC efficiency of 85.6% at 1.7 kW, and subsequent improvements increase the efficiency to 92.5% at 5 kW. These results demonstrate the design's strong potential in terms of both cost-effectiveness and performance. However, current research efforts primarily focus on static charging, while the more promising dynamic charging mode remains underexplored.

To further advance the prior work and ultimately enable wireless charging for the historical trolleys of the Belmont Trolley project [40], this study conducts an in-depth investigation into dynamic wireless power transfer (DWPT). First, a DWPT system based on a parallel synchronized multi-LCL-S compensation topology is proposed. The dynamic behavior of the coupling coefficient under motion is then analyzed, followed by the development of a prototype system. Finally, comprehensive experiments are carried out to evaluate both static and dynamic charging performance, thereby verifying the feasibility and effectiveness of the proposed approach.

TABLE I
Overview of wireless power transfer for railway applications

Year	Org.	Topo.	Air gap(cm)	Power(kW)	Eff.(%)	Ref.
2010	KAIST	SS	20	27	74.0	[14]
2011	KAIST	SS	20	27	74.0	[21]
2012	KAIST	SS	20	79.5	81.70	[22]
2013	KAIST	SS	20	–	91.0	[23]
2013	UA	LCL-T	–	6.0	94.0	[24]
2014	KAIST	SS	26	100	80.0	[25]
2015	RTRI	SP	7.5	38.7	73.0	[16]
2015	KAIST	SS	5	1000	82.70	[13]
2015	KAIST	SS	20	9.5	91.0	[26]
2017	SWJTU	SS	7	2.1	93.62	[27]
2017	JR Central	SS	13	12	89.0	[28]
2018	SWJTU	LCC	15	2.5	92.58	[29]
2019	CUT	LCC-C	15	27.8	93.0	[30]
2020	BIT	LCC-S	4	7.85	92.0	[31]
2020	KAIST	SS	23	12.7	90.8	[32]
2020	HIT	LCC-S	30	5.0	82.70	[33]
2021	SWJTU	LCC-LCC	3	1.2	92.20	[34]
2021	UNCC	LCL-S	12.7	1.7	85.6	[35]
2022	UNCC	LCL-S	12.7	5.0	92.5	[36]
2023	RTRI	SP	15	155.2	92.0	[37]
2024	RTRI	SS	15	150	90.0	[38]
2025	KRRI	SS	6	1000	90.1	[39]

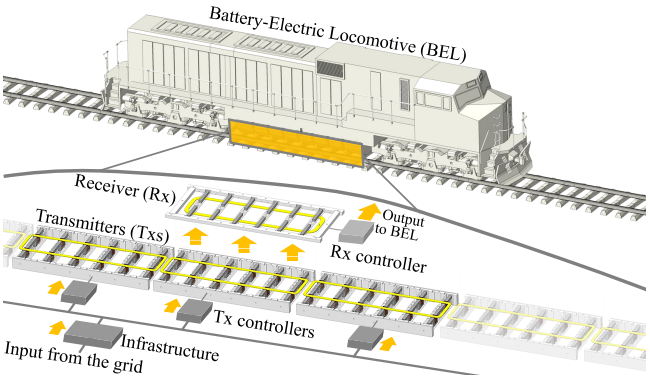

Fig. 1. Dynamic WPT system for locomotive with Txs between tracks and Rx in the vehicle.

The remainder of this paper is organized as follows. Section II analyzes the DWPT system, including the system concept, circuit topology, magnetic coupler design, dynamic coupling coefficient modeling and derivation, and prototype development. Section III focuses on static testing and analysis, covering misalignment effects, loss analysis, and static charging experiments. Section IV presents the dynamic testing and analysis, including dynamic charging performance, coupling coefficient variation, magnetic flux density distribution, and the influence of transmitter spacing. Section V discusses two application scenarios. Finally, Section VI concludes the paper and outlines directions for future work.

II. DWPT System for BELs

A. DWPT System Concept

Fig. 1 illustrates a simplified DWPT concept for BEL, consisting of ground side and locomotive side components [41]. The ground-side includes multiple modular transmitters (Txs), Tx controllers, and supporting infrastructure. The Txs and controllers are installed between the tracks, near the infrastructure at the charging site. The locomotive side includes at least one modular receiver (Rx) and an Rx controller. The Rx is mounted under the locomotive, while the Rx controller is placed inside the locomotive. The system draws power from the grid and converts it into high-frequency AC (85 kHz), which is then wirelessly transmitted via electromagnetic fields from the Txs to the Rx. The Rx controller converts the received AC to DC and delivers it to the locomotive's power system, where it is used to charge the battery. This article focuses solely on the WPT system from the Tx controller to the Rx controller.

B. DWPT Topology and W-I-Shaped Coupler

In this work, the LCL-S compensation topology is adopted to enhance power transfer capability and reduce the volt-ampere (VA) ratings. As illustrated in Fig. 2, the Tx side consists of three transmitters (Tx1, Tx2, and Tx3), each configured with a half LCL-S compensation network and

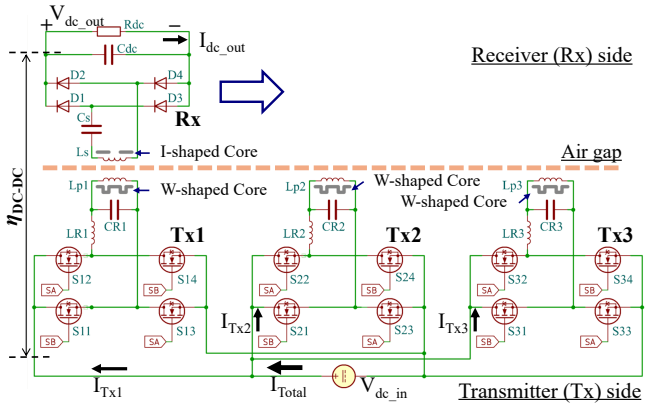

Fig. 2. DWPT circuit with an LCL-S compensation topology consists of three Txs and one Rx.

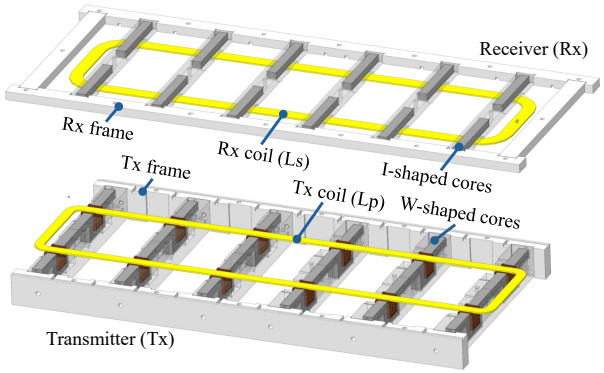

Fig. 3. W-I-shaped coupler with W-shaped cores on the Tx side and I-shaped cores on the Rx side.

connected in parallel to the DC source $V_{\mathrm{dc\_in}}$. Four MOSFET switches (Sx1 to Sx4, where "x" denotes the Tx number) are employed to generate an 85 kHz AC. The three transmitters share the same set of gate drive signals, and they can generate synchronous AC and magnetic fields. On the Rx side, a SiC diode full bridge module (D1 to D4) is used to rectify AC back to DC, then the DC is filtered by a capacitor C_{dc} and sent to the load resistor R_{dc}.

Fig. 3 illustrates the W-I-shaped magnetic coupler [41]. The upper section shows the Rx side, which consists of six pairs of I-shaped cores ("Rx core" in Fig. 2), an Rx coil ("L_{s}" in Fig. 2), and an Rx frame. The lower section presents the Tx side, which includes six W-shaped cores ("Tx core" in Fig. 2), a Tx coil ("L_{p}" in Fig. 2), and a Tx frame. The Rx-side I-shaped cores are composed of twenty-four I-100/25/25 bars, while the Tx-side W-shaped cores consist of twenty-four I-100/25/25 bars and twelve U-100/57/25 bars. The cores are made of 3C90 material from Ferroxcube, with a relative permeability of approximately 2300 [42]. Both coils are wound using 1500/38 Litz wire, comprising 1500 strands of 38 AWG (0.1 mm) wire. The air gap between the Tx and Rx sides is 12.7 cm.

C. Coupling Coefficient k_{mis} during Dynamic Charging

For DWPT used in railway systems, there should be multiple Txs to cover enough range to support dynamic charging. Fig. 4(a) demonstrates a model with one Rx coil and N Tx coils (Tx1 to TxN). The dots on the coils marked with "l", "c", and "r" represent the left center of the coil width, the center of the whole coil, and the right center of the coil width. Seven sections, from Position 1 (P1) to Position 7 (P7), indicate the positions of the Rx coil and Tx coils during the dynamic charging. For example, P1 corresponds to the "r" center of Rx coil aligning with the 'l" center of Tx1 coil. The distance between the "c" center of Rx coil and the "c" center of Tx1 coil is defined as the misalignment distance D_{mis}.

Fig. 4(b) illustrates how the coupling coefficient k_{mis} varies with the misalignment distance D_{mis} during the dynamic charging process. The k_{mis} axis represents the coupling coefficient between the Rx and all Txs, which can be considered the sum of the coupling coefficients between the Rx and each Tx in this paper. Based on seven positions, the whole process can be divided into six stages. (1) Approaching stage: From P1 to P2; (2) Falling stage: From P2 to P3; (3) Flat stage: From P3 to P4; (4) Rising stage: From P4 to P5; (5) Repeating stage: From P5 to P6; (6) Leaving stage: From P6 to P7.

D. Equations for Coupling Coefficient k_{mis}

There are some accurate closed-form formulations available for calculating the mutual inductance and coupling coefficient between rectangular coils [43]–[45]. However, these models typically assume simplified boundary conditions, such as a uniform air medium with constant permeability [43], [45], or a continuous magnetic plate close to the coils [44]. In this work, the receiver and transmitters employ discrete magnetic elements, making such analytical formulations no longer directly applicable. Deriving a new closed-form solution under these nonuniform magnetic conditions would be mathematically challenging. Therefore, in this paper, an engineering-oriented approach is adopted to estimate the coupling coefficient, providing a practical balance between analytical simplicity and modeling accuracy for systems with distributed magnetic structures.

Three assumptions are made in calculating the misalignment coupling coefficient k_{mis}: (1) Due to the distributed arrangement of magnetic cores, the electromagnetic field is nonuniform. Accurately modeling it under actual conditions would be overly complex and unnecessary; therefore, the electromagnetic fields of the Tx and Rx are assumed to be uniform, and the coupling coefficient is considered directly proportional to the overlapping length between the coils. (2) All Tx coils are assumed to have identical inductance values and geometric structures. (3) Since the lateral movement of the train is relatively small, misalignment is assumed to occur only along the track direction. With these three assumptions, a simplified analysis can be conducted to evaluate the system's dynamic performance.

Fig. 5 illustrates the parameters for calculating k_{mis} [41]. $L_{\mathrm{RxC\_lo}}$ is the outer length and $L_{\mathrm{RxC\_li}}$ is the inner length of the Rx coil; $L_{\mathrm{TxC\_lo}}$ is the outer length and $L_{\mathrm{TxC\_li}}$ is the inner length of the Tx coil; D_{mis} is the distance between the Rx and Tx1; D_{TT} is the distance between the two adjacent Tx coils. Using these parameters, the expressions of distance D_{mis} for each position are derived and listed in Table II. The relationship between the coupling coefficient k_{mis} and D_{mis} at each stage is derived as follows.

This article has been accepted for publication in IEEE Transactions on Industry Applications. This is the author's version which has not been fully edited and content may change prior to final publication. Citation information: DOI 10.1109/TIA.2026.3653938

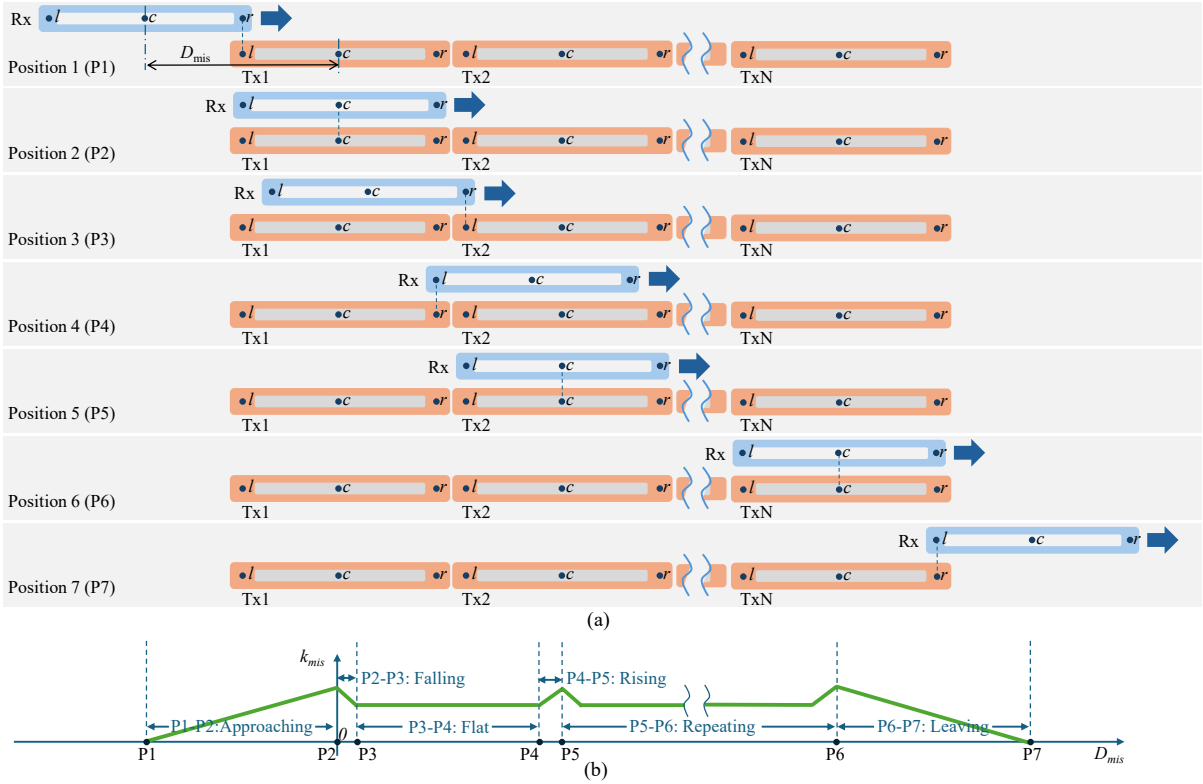

Fig. 4. Dynamic charging process: (a) Positions of the Rx coil during dynamic charging; (b) Coupling coefficient (k_{mis}) during dynamic charging.

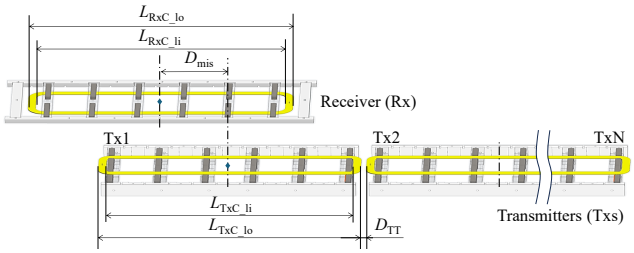

Fig. 5. Parameter definitions for calculating coupling coefficient k_{mis}.

At the "Approaching" stage, D_{mis} ranges from P1 to P2, k_{mis} can be calculated by:

$$k_{\text{mis}} = k_{\text{alg}}\left(1 + \frac{2D_{\text{mis}}}{L_{\text{RxC\_lo}} + L_{\text{RxC\_li}}}\right) \tag{1}$$

where k_{alg} is the coupling coefficient value when Rx is aligned with Tx. It will be obtained through experiments.

At the "Falling" stage, D_{mis} ranges from P2 to P3, k_{mis} can be calculated by:

$$k_{\text{mis}} = k_{\text{alg}}\left(1 - \frac{2(D_{\text{mis}} - (n-1)(L_{\text{TxC\_lo}} + D_{\text{TT}}))}{L_{\text{RxC\_lo}} + L_{\text{RxC\_li}}}\right) \tag{2}$$

where n is the No. of the Tx, and $n \in \{1, 2, \ldots, N-1\}$, N is the total number of Txs.

At the "Flat" stage, D_{mis} ranges from P3 to P4, k_{mis} is a constant value and can be calculated by:

$$k_{\text{mis}} = k_{\text{alg}}\left(1 - \frac{2(D_{\text{TT}} + L_{\text{TxC\_lo}} - L_{\text{TxC\_li}})}{L_{\text{RxC\_lo}} + L_{\text{RxC\_li}}}\right) \tag{3}$$

At the "Rising" stage, D_{mis} ranges from P4 to P5, k_{mis} can be calculated by:

$$k_{\text{mis}} = k_{\text{alg}}\left(1 + \frac{2(D_{\text{mis}} - (n-1)(L_{\text{TxC\_lo}} + D_{\text{TT}}))}{L_{\text{RxC\_lo}} + L_{\text{RxC\_li}}}\right) \tag{4}$$

TABLE II
POSITIONS AND RX-TX1 DISTANCES DURING DYNAMIC CHARGING.

Position	Rx-Tx1 Distance D_{mis}
P1	$-\frac{L_{\text{TxC\_lo}}+L_{\text{TxC\_li}}}{4}-\frac{L_{\text{RxC\_lo}}+L_{\text{RxC\_li}}}{4}$
P2	0 or $(n-1)(L_{\text{TxC\_lo}}+D_{\text{TT}})$
P3	$(n-1)(L_{\text{TxC\_lo}}+D_{\text{TT}})+D_{\text{TT}}+\frac{L_{\text{TxC\_lo}}-L_{\text{TxC\_li}}}{2}$
P4	$(n-1)(L_{\text{TxC\_lo}}+D_{\text{TT}})+\frac{L_{\text{RxC\_lo}}+L_{\text{RxC\_li}}}{4}$ $+\frac{L_{\text{TxC\_lo}}+L_{\text{TxC\_li}}}{4}$
P5	$(n-1)(L_{\text{TxC\_lo}}+D_{\text{TT}})+\frac{L_{\text{RxC\_lo}}+L_{\text{RxC\_li}}}{4}$ $+\frac{L_{\text{TxC\_lo}}+L_{\text{TxC\_li}}}{4}+\frac{L_{\text{TxC\_lo}}-L_{\text{TxC\_li}}}{2}+D_{\text{TT}}$
P6	$(N-2)(L_{\text{TxC\_lo}}+D_{\text{TT}})+\frac{L_{\text{RxC\_lo}}+L_{\text{RxC\_li}}}{4}$ $+\frac{L_{\text{TxC\_lo}}+L_{\text{TxC\_li}}}{4}+\frac{L_{\text{TxC\_lo}}-L_{\text{TxC\_li}}}{2}+D_{\text{TT}}$
P7	$(N-2)(L_{\text{TxC\_lo}}+D_{\text{TT}})+\frac{L_{\text{RxC\_lo}}+L_{\text{RxC\_li}}}{4}$ $+\frac{3(L_{\text{TxC\_lo}}+L_{\text{TxC\_li}})}{4}+\frac{L_{\text{TxC\_lo}}-L_{\text{TxC\_li}}}{2}+D_{\text{TT}}$

At the "Repeating" stage, k_{mis} repeats the stage from P5 to P6 periodically.

At the "Leaving" stage, D_{mis} ranges from P6 to P7, k_{mis} can be calculated by:

$$k_{\text{mis}} = k_{\text{alg}}\left(1 - \frac{2(D_{\text{mis}} - (N-1)(L_{\text{TxC\_lo}} + D_{\text{TT}}))}{L_{\text{RxC\_lo}} + L_{\text{RxC\_li}}}\right) \tag{5}$$

where N is the total number of Txs.

TABLE III
EXPERIMENTAL TTSR MODEL PARAMETERS FOR DYNAMIC CHARGING.

Parameter	Symbol	Value
Total Tx number	N	3
Rx coil outer length	$L_{\mathrm{RxC\_lo}}$	125.73 cm
Rx coil inner length	$L_{\mathrm{RxC\_li}}$	118.11 cm
Tx coil outer length	$L_{\mathrm{TxC\_lo}}$	124.46 cm
Tx coil inner length	$L_{\mathrm{TxC\_li}}$	119.38 cm
Space between Txs	D_{TT}	0
Tx capacitor	C_{R}	48.89 nF
Rx inductor	L_{s}	175.30 μH
Rx capacitor	C_{s}	20 nF
Tx inductor	$L_{\mathrm{p}}, L_{\mathrm{R}}$	71.70 μH
Aligned coupling coefficient	k_{alg}	0.2327
Switching frequency	f	85 kHz

In this work, a three-transmitter and single-receiver (TTSR) model is used for the experiment and the model's parameters are listed in Table III. By substituting the values into equations from (1) to (5), the k_{mis} for the TTSR WPT system can be calculated by (6).

$$k_{\mathrm{mis}} = \begin{cases} 0.2327\left(1+\dfrac{D_{\mathrm{mis}}}{121.92}\right), \\ \quad \text{if} \quad -121.92 < D_{\mathrm{mis}} \le 0 \\ 0.2327\left(1-\dfrac{D_{\mathrm{mis}}-124.46n+124.46}{121.92}\right), \\ \quad \text{if} \quad 124.46(n-1) < D_{\mathrm{mis}} \le 124.46n-121.92 \\ 0.2279, \\ \quad \text{if} \quad 124.46n-121.92 < D_{\mathrm{mis}} \le 124.46n-2.54 \\ 0.2327\left(1+\dfrac{D_{\mathrm{mis}}-124.46n+124.46}{121.92}\right), \\ \quad \text{if} \quad 124.46n-2.54 < D_{\mathrm{mis}} \le 124.46n \\ 0.2327\left(1-\dfrac{D_{\mathrm{mis}}-248.92}{121.92}\right), \\ \quad \text{if} \quad 248.92 < D_{\mathrm{mis}} \le 370.84 \end{cases} \tag{6}$$

where $n \in \{1, 2\}$ is the order of Tx, and D_{mis} is the Rx-Tx1 distance. For clarity, the unit of D_{mis} (cm) is omitted.

Fig. 6 shows the equivalent circuit, subject to the design constraints $j\omega L_{\mathrm{R}} = -\frac{1}{j\omega C_{\mathrm{R}}}$, $L_{\mathrm{R}} = L_{\mathrm{p}}$, and $j\omega L_{\mathrm{S}} = -\frac{1}{j\omega C_{\mathrm{S}}}$.

The input and output voltages are derived as follows:

$$V_{\mathrm{in}} = I_{\mathrm{in}} j\omega L_{\mathrm{R}} + (I_{\mathrm{in}} - I_1)\frac{1}{j\omega C_{\mathrm{R}}} = -I_1 \frac{1}{j\omega C_{\mathrm{R}}} \tag{7}$$

$$V_{\mathrm{o}} = I_1 j\omega M + I_2\left(j\omega L_{\mathrm{S}} + \frac{1}{j\omega C_{\mathrm{S}}}\right) = I_1 j\omega M \tag{8}$$

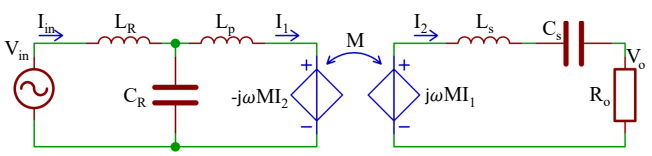

Fig. 6. LCL-S compensation topology equivalent circuit.

The mutual inductance M is defined as:

$$M = k\sqrt{L_{\mathrm{p}} L_{\mathrm{s}}} \tag{9}$$

where k is the coupling coefficient.

Combining (7), (8), and (9) yields:

$$V_{\mathrm{o}} = k V_{\mathrm{in}}\, \omega^2 \sqrt{L_{\mathrm{p}} L_{\mathrm{s}}}\, C_{\mathrm{R}} \tag{10}$$

Therefore, the DC output voltage can be expressed as:

$$V_{\mathrm{dc\_out}} = k\, V_{\mathrm{dc\_in}}\, \omega^2 \sqrt{L_{\mathrm{p}} L_{\mathrm{s}}}\, C_{\mathrm{R}} \tag{11}$$

By combining (6) and (11), for a TTSR model, the DC output voltage $V_{\mathrm{dc\_out}}$ can be calculated by (12):

$$V_{\mathrm{dc\_out}} = \begin{cases} 0.3639\left(1+\dfrac{D_{\mathrm{mis}}}{121.92}\right) V_{\mathrm{dc\_in}}, & \text{if } -121.92 < D_{\mathrm{mis}} \le 0 \\ 0.3639\left(1-\dfrac{D_{\mathrm{mis}}}{121.92}\right) V_{\mathrm{dc\_in}}, & \text{if } 0 < D_{\mathrm{mis}} \le 2.54 \\ 0.3562 V_{\mathrm{dc\_in}}, & \text{if } 2.54 < D_{\mathrm{mis}} \le 121.92 \\ 0.3639\left(1+\dfrac{D_{\mathrm{mis}}-124.46}{121.92}\right) V_{\mathrm{dc\_in}}, & \text{if } 121.92 < D_{\mathrm{mis}} \le 124.46 \\ 0.3639\left(1-\dfrac{D_{\mathrm{mis}}-124.46}{121.92}\right) V_{\mathrm{dc\_in}}, & \text{if } 124.46 < D_{\mathrm{mis}} \le 127 \\ 0.3562 V_{\mathrm{dc\_in}}, & \text{if } 127 < D_{\mathrm{mis}} \le 246.38 \\ 0.3639\left(1+\dfrac{D_{\mathrm{mis}}-248.92}{121.92}\right) V_{\mathrm{dc\_in}}, & \text{if } 246.38 < D_{\mathrm{mis}} \le 248.92 \\ 0.3639\left(1-\dfrac{D_{\mathrm{mis}}-248.92}{121.92}\right) V_{\mathrm{dc\_in}}, & \text{if } 248.92 < D_{\mathrm{mis}} \le 370.84 \end{cases} \tag{12}$$

where D_{mis} is the Rx-Tx1 distance. It is worth noting that (6) contains only six terms, while (8) has eight terms. This is because different values of n (i.e., 1 and 2) are substituted into (6) to derive the result.

Similarly, by combining (6) and (11), and setting N= 1 (n = 0), the output voltage $V_{\mathrm{dc\_out}}$ of a single-transmitter and single-receiver (STSR) model can be predicted by (13).

$$V_{\mathrm{dc\_out}} = \begin{cases} 0.3639(1+\dfrac{D_{\mathrm{mis}}}{121.92}) V_{\mathrm{dc\_in}}, & -121.92 < D_{mis} \le 0 \\ 0.3639(1-\dfrac{D_{\mathrm{mis}}}{121.92}) V_{\mathrm{dc\_in}}, & 0 < D_{mis} \le 121.92 \end{cases} \tag{13}$$

Fig. 7 illustrates the overall output voltage trends. The STSR waveform calculated from (13) exhibits a triangular shape, indicating the general trend of voltage rising as Rx approaches Tx, peaking at alignment, and decreasing as Rx moves away. The TTSR waveform derived from (12) features a rising slope, a flat region while Rx passes over the Txs, and a falling slope, with three small peaks observed at alignment.

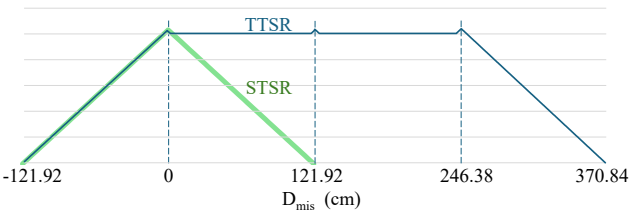

Fig. 7. Calculated output voltage trends under misalignment for STSR and TTSR

TABLE IV
DESIGNED AND MEASURED PARAMETERS OF PROTOTYPE.

Component	Parameter	Designed	Measured
Tx coil (μH)	L_{p1}	71.70	72.64
	L_{p2}		71.63
	L_{p3}		71.71
Tx Inductor (μH)	L_{R1}	71.70	72.64
	L_{R2}		71.63
	L_{R3}		71.71
Tx Capacitor (nF)	C_{R1}	48.89	48.26
	C_{R2}		48.94
	C_{R3}		48.90
Rx coil (nH)	L_s	175.30	176.43
Rx Capacitor (nF)	C_s	20	20
DC Capacitor (nF)	C_{dc}	120	120
Load resistor (Ω)	R_{dc}	5-50	5-50
Air gap (cm)	D_A	12.7	12.7
Frequency (kHz)	f	85	85

E. Prototype and Parameters

The TTSR prototype used for dynamic performance testing is shown in Fig. 8, consisting of the Tx side, the Rx side, and various test equipment. The Tx side includes three Txs (each comprising a Tx coupler and an inverter), a digital signal processor (DSP, TI LAUNCHXL-F28379D), and a section of track. The Txs are positioned between the tracks, with the DSP generating the switching frequency signals. The track spacing is 143.5 cm. The Rx side comprises a Rx coupler and rectifier mounted on a movable platform, along with an LED bar. The Rx coupler is suspended beneath the platform, while the rectifier is mounted on top. The platform has four wheels, a steel frame, and a wooden panel. The LED bar, installed on the platform frame, indicates the power transfer status. The test setup also includes a DC power source (Chroma 62100H-1000), an electronic load (Chroma 63200A), a power analyzer (TEKTRONIX PA3000), and two oscilloscopes (Tektronix MDO3054, only one shown in the picture). The corresponding parameters are listed in Table IV.

III. Static Test and Analysis

A. Misalignment Experiment and Analysis

For the static misalignment test, only Tx1 and Rx in the TTSR model are energized, making it an STSR model. The input voltage V_{dc_in} is set to 705 V, and the load resistance R_{dc} is fixed at 21 Ω. The resulting waveforms are presented in Fig. 9, where Fig. 9(a) displays the waveforms on the Tx side, and Fig. 9(b) shows those on the Rx side. Due to the use of two separate oscilloscopes, dashed lines are added in each figure to indicate the time synchronization points.

The experimental results of the STSR model under misalignment conditions are shown in Fig. 10. The lower part demonstrates the positions of Rx and Tx1. During the test, the Rx moves above the Tx1 from left to right with a step of 5.08 cm. The misalignment distance between Rx and Tx1 (D_{mis}) is from −137.16 to +137.16 cm. The distance between the Rx coil and Tx1 coil (air gap) is 12.7 cm.

The middle part presents the input power P_{dc_in}, output power P_{dc_out}, and DC-DC efficiency $\eta_{DC\text{-}DC}$ versus D_{mis}. The waveforms of P_{dc_in} and P_{dc_out} show a steep peak shape. When Rx and Tx1 are aligned, they reach the maximum value simultaneously, then drop rapidly on both sides, even if the D_{mis} is not large, which means the system power is susceptible to misalignment. The waveform of $\eta_{DC\text{-}DC}$ shows a table shape with a flat top. It also reaches the peak when Rx and Tx1 are aligned, but the drop is not obvious when the D_{mis} is small, which implies that efficiency is not sensitive to misalignment. $\eta_{DC\text{-}DC}$ reaches a maximum value of 94.73%, corresponding to the maximum P_{dc_in} of 3102.26 W and the maximum P_{dc_out} of 2938.69 W. In addition, the efficiency curve demonstrates that the system maintains a high efficiency of 90% even when the D_{mis} is 40 cm, which is approximately 1/3 of the total length of the Tx coil (124.46 cm). This highlights the system's excellent anti-misalignment performance in maintaining efficiency.

The upper part displays the output voltage V_{dc_out}, input current I_{Tx1}, output current I_{dc_out}, and the calculated

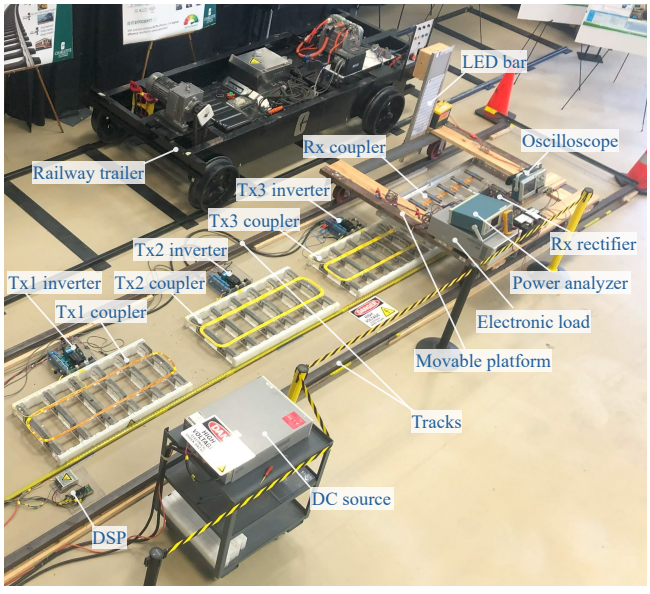

Fig. 8. Prototype of the dynamic WPT system with three Txs and one Rx.

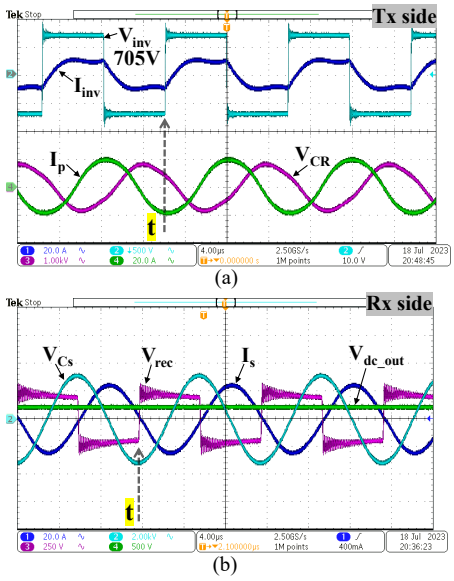

Fig. 9. STSR model experimental waveform at input voltage of 705 V.

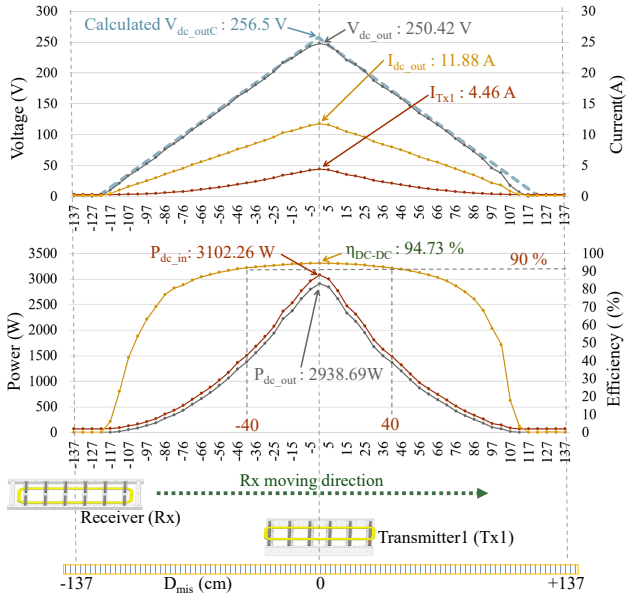

Fig. 10. STSR model misalignment experimental results at input voltage 705 V and load resistor 21 Ω.

output voltage V_{dc_outC}. The V_{dc_out} and I_{dc_out} waveforms resemble triangles. This suggests that the coupling coefficient or mutual inductance is linearly related to misalignment. Meanwhile, the input current I_{Tx1} exhibits a parabolic shape, resulting from the constant input voltage and fixed load resistance. The results shows the maximum V_{dc_out} of 250.42 V, the maximum I_{dc_out} of 11.88 A, and the maximum I_{Tx1} of 4.46 A during test.

Furthermore, the calculated V_{dc_outC} waveform shows a high level of consistency with the experimental measurement. Both waveforms display a triangular profile, and the peak voltage differs by only 2.42%. This consistency confirms that the theoretical model accurately captures the behavior of the STSR configuration under misalignment conditions, thereby validating the proposed calculation method through experimental verification. However, it should be noted that a sharp peak appears in the calculated waveform but is not evident in the experimental results. This discrepancy primarily arises from the simplified analytical model, which neglects the coil width, as well as from measurement precision limitations during the experiment.

B. Loss Analysis

The system loss analysis is conducted through two simulations. Circuit-related losses, including inverter switching loss, rectifier loss, coil loss, Tx compensation loss, Rx compensation loss, and other component and wiring loss, are evaluated using an STSR model in PLECS, whereas magnetic core losses (comprising both hysteresis and eddy current losses) are quantified using an Ansys Maxwell model. As shown in Fig. 11, the simulated maximum efficiency of the STSR model reaches 95.31% under perfect alignment, which is slightly higher than the corresponding experimental value. Within the total power loss of 4.69%, the coil loss constitutes the largest portion, at 2.65%, indicating that coil optimization could further improve the overall efficiency. Other losses, such as cable and PCB copper losses as well as eddy current

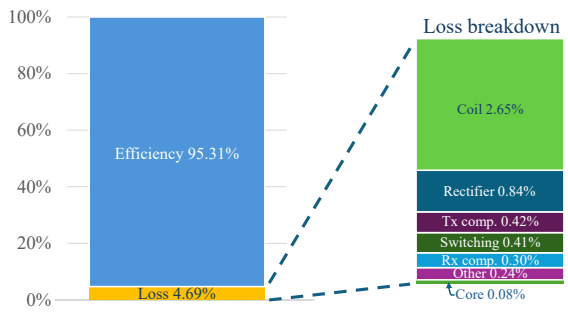

Fig. 11. Simulated maximum efficiency and loss distribution of the STSR model.

losses in the track and steel trailer, contribute only 0.24%. The magnetic core losses in ferrite bars are only 0.08%.

C. Static Charging Efficiency Map

Efficiency is a critical performance indicator for WPT systems. To investigate the efficiency characteristics, additional experiments are conducted with load resistance R_{dc} varying from 15 to 34 Ω and input voltage V_{dc_in} ranging from 100 to 500 V, with the results shown in Fig. 12. From the perspective of input voltage, higher voltages generally correspond to increased efficiency. For instance, when the V_{dc_in} is 100 V, the efficiency is from 89% to 90%; when the V_{dc_in} is 500 V, the efficiency is from 93.5% to more than 94%. From the perspective of load resistors, there is an optimal range, efficiency peaks within this range, and decreases as it deviates. It can be observed from the figure that the optimal efficiency, exceeding 94%, is achieved when the voltage is above 450 V and the resistance is between 15 and 23 Ω. In addition, the system also features an efficiency of more than 92% in most areas within the tested range, which is a notable advantage. These findings provide valuable references for optimizing the system and guiding its future applications.

IV. Dynamic Test and Analysis

A. Dynamic Test and Analysis for Zero D_{TT}

The dynamic tests are performed using the TTSR model, with the spacing between adjacent Tx coils (D_{TT}) set to 0 cm. The test conditions are as follows: input power is 3 kW, input DC voltage (V_{dc_in}) is 500 V, and load resistance (R_{dc}) is 15 Ω. The distance between the Rx and Tx2 serves as the reference position. When the Rx is aligned with Tx2, the

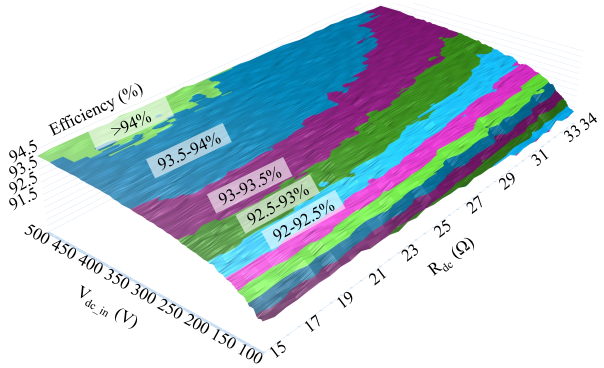

Fig. 12. Efficiency map with input voltage V_{dc_in} from 100 to 500 V and load resistor R_{dc} from 15 to 34 Ω.

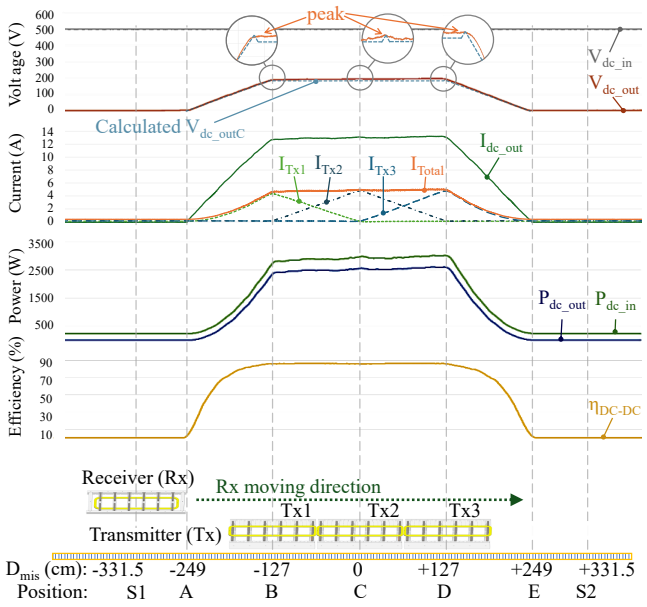

Fig. 13. TTSR model dynamic experimental results at input power P_{dc_in}=3 kW, input voltage V_{dc_in}=500 V, and load resistor R_{dc}=15 Ω.

misalignment distance (D_{mis}) is defined as 0 cm, and D_{mis} ranges from -331.5 cm to +331.5 cm.

The experimental results are reported in Fig. 13. The lower part illustrates the positions of Rx and the Txs, showing that Rx moves from left to right above the three Txs. The upper part shows the measurements, including voltage, current, power, and efficiency. The details are described below.

(1) At position S1 (D_{mis} = −331.5 cm), no current is induced in the Rx coil and no power is transferred, resulting in zero efficiency. However, small currents remain in the Tx coils due to circuit losses, leading to an input power of about 230 W.

(2) At position A (D_{mis} = −249 cm), the Rx coil begins to overlap with Tx1. A current is induced in the Rx coil, increasing I_{Tx1}, while Tx2 and Tx3 still carry only loss currents. Consequently, the system starts generating output voltage, current, and power, and the DC–DC efficiency becomes nonzero.

(3) From position A to position B (D_{mis} from −249 cm to −127 cm), the Rx continues to approach Tx1. As more of the Rx coil overlaps with Tx1, V_{dc_out}, I_{dc_out}, P_{dc_out}, and η_{DC-DC} increase progressively.

(4) At position B (D_{mis} = −127 cm), the Rx coil is fully aligned with Tx1. I_{Tx1} and the Rx current both reach their peak values, and the system achieves maximum V_{dc_out}, I_{dc_out}, P_{dc_out}, and η_{DC-DC}. Meanwhile, I_{Tx2} begins to rise as the Rx approaches Tx2. A small voltage peak is observed at this alignment, as highlighted in the enlarged view of the V_{dc_out} waveform, although it is not prominent due to geometric tolerances in the setup.

(5) From position B to position C (D_{mis} from −127 cm to 0 cm), the Rx moves between Tx1 and Tx2, aligning partially with both. I_{Tx1} decreases while I_{Tx2} increases, and Tx2 begins delivering more energy. The system maintains stable operation with high output power and efficiency.

(6) At position C (D_{mis} = 0 cm), the Rx coil aligns perfectly with Tx2. I_{Tx2} reaches its maximum, I_{Tx1} drops nearly to zero, and I_{Tx3} starts to rise. The system continues to operate stably at maximum output power and efficiency. Another small voltage peak can be observed on the waveform.

(7) From position C to position E (D_{mis} from 0 cm to 249 cm), the system behavior mirrors that of the A–C transition. As the Rx moves away from Tx2 and aligns with Tx3, the input current shifts from Tx2 to Tx3, and the output power and efficiency decrease gradually after reaching a peak at position D.

(8) From position E to position S2 (D_{mis} from 249 cm to 331.5 cm), the Rx moves away from all Txs, and the output power drops to zero.

The experimental results further demonstrate that the system can maintain the highest level of efficiency during dynamic charging, with both system input and output power increasing and decreasing smoothly at the beginning and end of the charging process. These characteristics are beneficial for practical applications. Additionally, it can be seen in the voltage section, the calculated V_{dc_outC} waveform closely matches the experimental results in waveform characteristics. This strong correlation confirms that the proposed theoretical model remains valid for the TTSR configuration under dynamic conditions, further verifying the accuracy and practical applicability of the calculation method.

It is worth noting that, due to circuit losses within and between the Txs, as well as the presence of unloaded Txs during operation, the system's maximum efficiency in the dynamic experiments is approximately 89%, which is lower than the peak efficiency of 94.73% achieved under static conditions. Potential approaches to further improve efficiency include optimizing the Tx and Rx circuit design to reduce impedance losses and implementing an adaptive control strategy to disable inactive Txs during operation.

B. Dynamic Coupling Coefficient (k) Analysis

In WPT systems, misalignment is a critical factor influencing output stability. Compared with EVs or small electronic devices, misalignment in electric trains exhibits unique characteristics. The railway tracks effectively constrain lateral misalignment, while the use of multiple series-connected transmitters helps mitigate the impact of longitudinal misalignment. In practical dynamic charging scenarios, vibrations induced by train motion inevitably introduce coil misalignment. Therefore, it is essential to analyze this effect.

As shown in Fig. 14 (a) to (h), the coil misalignment can be decomposed into six degrees of freedom, including three translational directions in Fig. 14(a): x-direction (lateral, perpendicular to the track), y-direction (longitudinal, along the track), and z-direction (vertical, perpendicular to the ground); as well as three rotational directions in Fig. 14(b): x-axis rotation, y-axis rotation, and z-axis rotation. Any practical misalignment condition can be regarded as a combination of these six basic freedoms.

Fig. 15 shows the effect of different misaligned freedoms on the coupling coefficient in the STSR model based on finite element analysis. For clarity of comparison, the figure presents the misaligned coupling coefficient (k_{mis}), expressed

This article has been accepted for publication in IEEE Transactions on Industry Applications. This is the author's version which has not been fully edited and content may change prior to final publication. Citation information: DOI 10.1109/TIA.2026.3653938

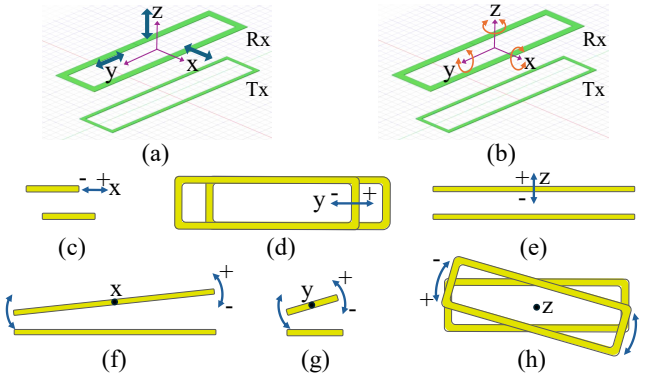

Fig. 14. Coil misalignment can be decomposed into six degrees of freedom: (a) three degrees of translation freedom, (b) three degrees of rotation freedom, (c) x-direction translation, (d) y-direction translation, (e) z-direction translation, (f) x-axis rotation, (g) y-axis rotation, (h) z-axis rotation.

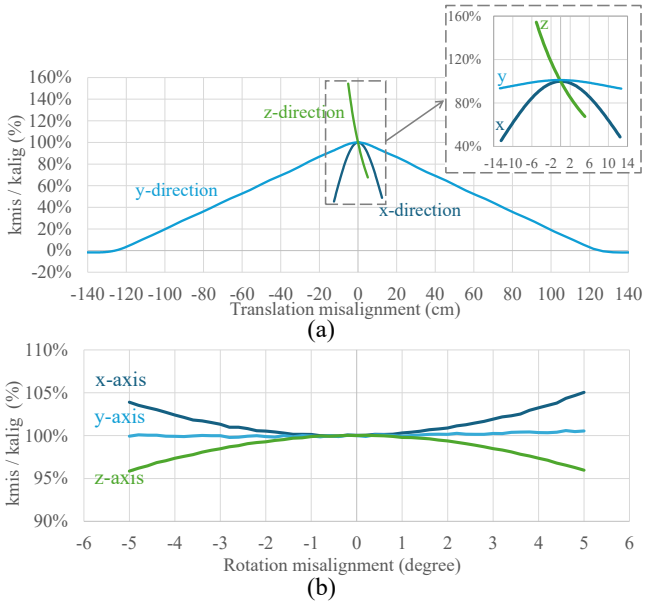

Fig. 15. Effects of six misalignment freedoms on the coupling coefficient (k): (a) three translation misalignment freedoms, (b) three rotation misalignment freedoms.

as a percentage relative to perfect alignment (k_{alg}). AS displayed in Fig. 15(a), the misalignment along the z-direction has the most significant impact on the coupling coefficient, followed by the x-direction, while the y-direction has the least effect. As analyzed earlier, misalignment along the y-direction can be mitigated by arranging multiple transmitters in series. Z-direction misalignment can be alleviated through the precise design of the receiver mounting brackets and by maintaining a uniform transmitter height. X-direction misalignment can be reduced by avoiding the installation of transmitters at curved sections of the track. For rotational misalignment, shown in Fig. 15(b), x-axis and z-axis rotations have comparable effects but with opposite trends: x-axis rotation increases the coupling coefficient, whereas z-axis rotation decreases it. Meanwhile, rotation around the y-axis has a negligible influence. Since x-axis rotation may result from track slope variations and z-axis rotation from curved sections, transmitters should therefore be avoided at locations with slopes and curves.

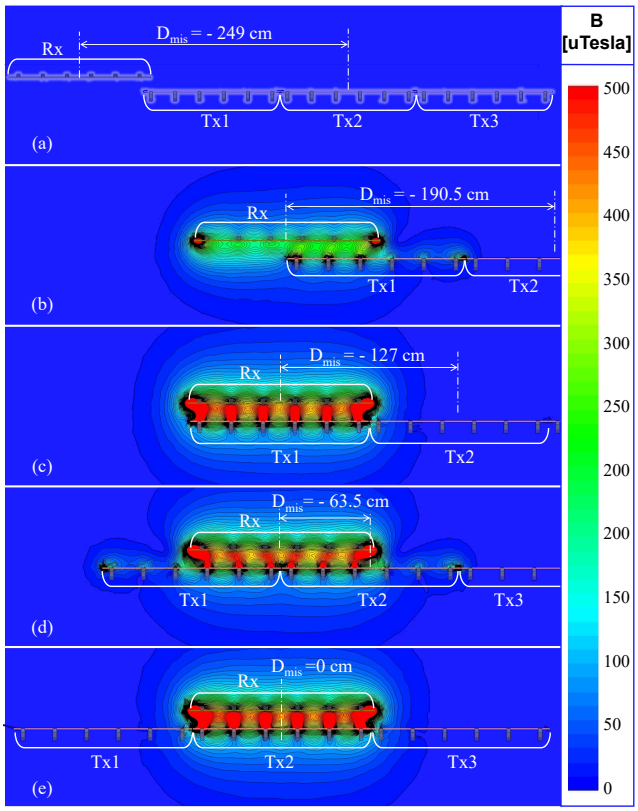

Fig. 16. Magnetic flux density (B) during dynamic charging: (a) D_{mis} is -249 cm; (b) D_{mis} is -190.5 cm; (c) D_{mis} is -127 cm; (d) D_{mis} is -63.5 cm; (e) D_{mis} is 0 cm.

C. Magnetic Flux Density (B) Analysis

The magnetic flux density (B) is a key parameter in WPT. To better understand the dynamic charging process, the magnetic flux density is simulated using finite element analysis, with the results shown in Fig. 16. For clarity, only the coils and magnetic cores are displayed. These simulations illustrate how the flux distribution evolves as the Rx moves relative to the Txs during charging. At D_{mis} = -249 cm in Fig. 16(a), only loss currents exist in the Tx coils, resulting in very low flux density. At D_{mis} = -190.5 cm in Fig. 16(b), the Rx partially overlaps Tx1, concentrating flux in the overlapping region. At D_{mis} = -127 cm in Fig. 16(c), full alignment with Tx1 maximizes flux density, coupling, power, and efficiency. At D_{mis} = -63.5 cm in Fig. 16(d), the Rx spans Tx1 and Tx2, maintaining high coupling and output. Finally, at D_{mis} = 0 cm in Fig. 16(e), alignment with Tx2 produces another peak in flux, power, and efficiency.

D. Dynamic Test and Analysis for Various D_{TT}

The previous analysis and tests demonstrate the system's performance with D_{TT} set to 0 cm. In practical applications, however, this spacing may vary. To evaluate performance under more realistic conditions, additional tests are conducted with D_{TT} ranging from 0 to 106.68 cm in 5.08 cm increments. Fig. 17 illustrates the input power P_{dc_in}, output power P_{dc_out}, and DC-DC efficiency $\eta_{DC\text{-}DC}$ at four representative D_{TT} values. The results show stable waveforms when D_{TT} = 0 cm. As D_{TT} increases, sags appear in the waveforms, becoming wider and deeper with larger spacing. These sags

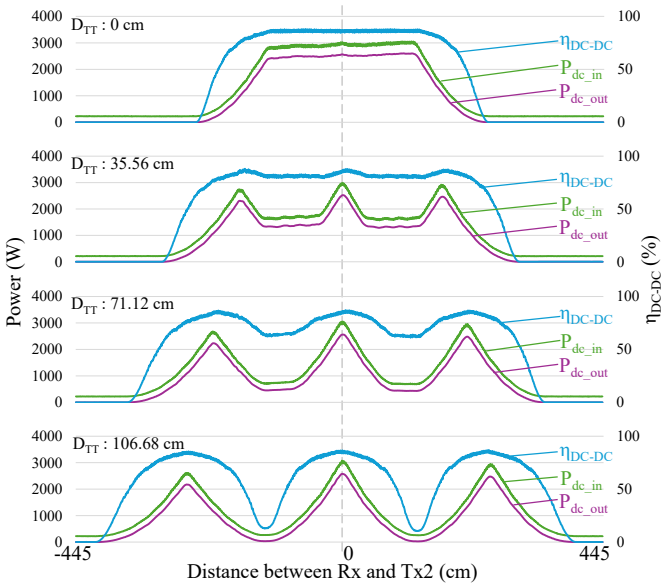

Fig. 17. Input power, output power, and efficiency at various D_{TT}.

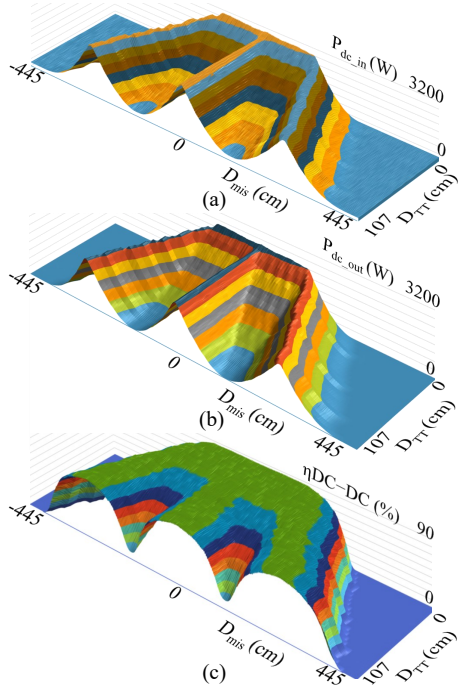

Fig. 18. 3D surface graph of power and efficiency at various D_{TT}: (a) Input power $P_{\mathrm{dc\_in}}$ vs. D_{mis} and D_{TT}; (b) Output power $P_{\mathrm{dc\_out}}$ vs. D_{mis} and D_{TT}; (c) DC-DC efficiency $\eta_{\mathrm{DC\text{-}DC}}$ vs. D_{mis} and D_{TT}.

indicate fluctuations in power and efficiency, which can degrade system performance. This suggests that additional filtering in the secondary circuit may be needed to maintain stable charging if D_{TT} is not zero.

Fig. 18 presents the results for all tested D_{TT} values from 0 to 106.68 cm. Specifically, Fig. 18(a) shows the input power $P_{\mathrm{dc\_in}}$, Fig. 18(b) shows the output power $P_{\mathrm{dc\_out}}$, and Fig. 18(c) shows the DC–DC efficiency $\eta_{\mathrm{DC\text{-}DC}}$, all as functions of D_{mis} and D_{TT}. When $D_{\mathrm{TT}} = 0$, both input and output powers are highly stable, and efficiency reaches its maximum, representing the system's optimal state. As D_{TT} increases, peak values are still achieved when the Rx aligns with a Tx; however, pronounced sags appear during transitions between Txs, becoming more significant at larger D_{TT}. This indicates that input and output powers are highly sensitive to variations in D_{TT}. In Fig. 18(a) and (b), the input and output powers form an E-shaped ridge with wide valleys. In contrast, the efficiency in Fig. 18(c) decreases only slightly under misalignment, with narrower valleys and a broader E-shaped peak. This demonstrates that the system maintains high efficiency across a wider range of D_{TT} values.

V. Case Study

A. Belmont Trolley

The Belmont Trolley project [40], located in Belmont, North Carolina, provides a representative case study for implementing WPT in light rail transit. The project aims to restore a historic 2.3 km trolley line with five stations and an average speed of 6.71 m/s, enabling low-emission operation and improving connectivity between downtown Belmont and Abbey College. Conventional OCS are infeasible due to infrastructure constraints, and retrofitting existing DC-motor trolleys is undesirable as it would compromise their historic character. The project proposes pairing each trolley with a compact battery trailer housing a 40 kWh (80%, 32 kWh usable) traction battery, which supplies DC power during operation. With a single round trip consuming approximately 13.94 kWh, only two round trips are possible per charge, insufficient for the required four daily trips. To address this, the project applies WPT to recharge the battery during scheduled dwell times at stations, as shown in Fig. 19, enabling continuous operation.

In the proposed configuration, one charging unit is installed at both the first and last stations. Each unit integrates three transmitting coils, while the trailer is equipped with two receiver coils, providing a charging power of 8 kW. During a 40-minute dwell period at each end station, the system delivers approximately 5.33 kWh to the battery, yielding a total of 10.66 kWh of recharge per round trip. Fig. 20 illustrates the battery's usable energy profile over four round trips in a single day. The upper curve represents the usable battery energy, with values before and after each charging event indicated. Initially, the available energy is 32 kWh. During operation, energy is consumed when passing intermediate stations (S2, S3, and S4) and replenished at the first (S1) and last (S5) stations. At the conclusion of the fourth trip, the battery retains 13.57 kWh, confirming that station-based WPT enables the trolley to meet the required daily schedule. After service concludes, the battery continues to charge at S1 until it is fully replenished, thereby ensuring

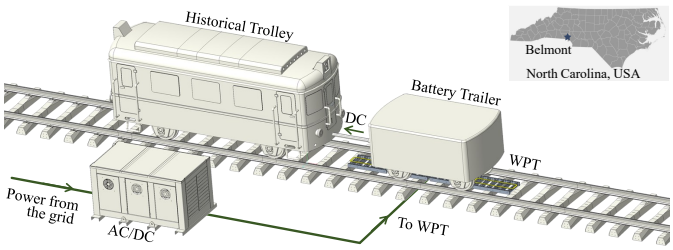

Fig. 19. Concept of WPT charging solution for the Belmont Trolley project.

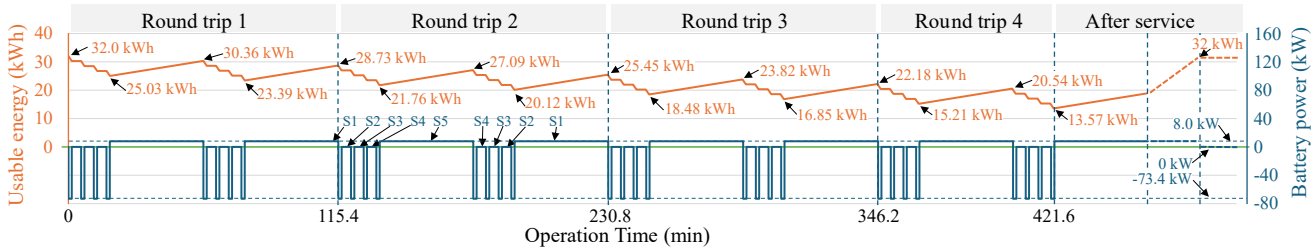

Fig. 20. Battery energy and battery power during one-day operation.

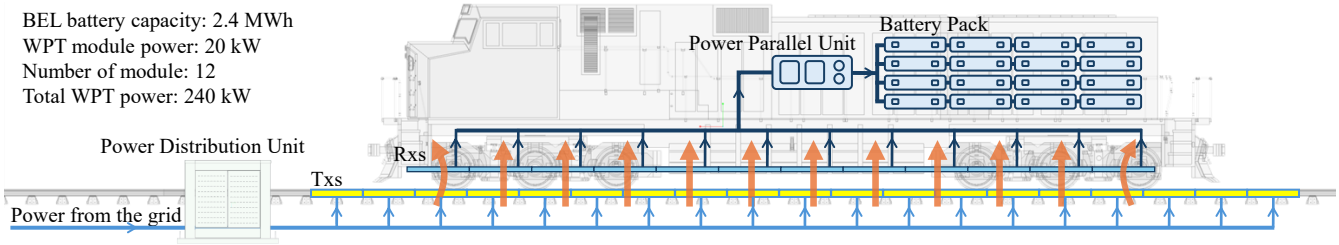

Fig. 21. Concept of full-scale WPT application for battery electric locomotive (BEL).

readiness for the next day's operation. The lower curve shows the instantaneous battery power, highlighting the charging at the first (S1) and last (S5) stations, as well as the discharging at the intermediate stations (S2, S3, and S4).

B. BEL Charging

Full-scale battery electric locomotives (BELs) require 2.4–7 MWh batteries [46], [47], while the 5 kW WPT module considered here is clearly insufficient, making scaling to higher power levels essential. Based on proven EV WPT designs [48], this work can increase a single module's capacity to 20 kW using high-voltage/current semiconductors, high-power Litz wire coils, and advanced magnetic components [49]–[51], with parallel receiver circuits enabling stacked high-power transmission.

The concept is illustrated in Fig. 21, which presents a switcher BEL with a 2.4 MWh battery capacity. With each module rated at 20 kW, twelve modules in parallel provide a total of 240 kW, enabling the battery to be fully recharged within 10 hours. Compared with the 177 kW cable-based charging system reported in [47], the proposed multi-module WPT approach not only achieves higher charging power but also simplifies the process by eliminating manual cable connections, reducing preparation time, and enabling flexible opportunity charging during idle periods. These advantages collectively provide a foundation for reducing the required battery capacity while maintaining operational reliability in railway applications.

VI. Conclusion and Future Work

A DWPT system for battery electric locomotives with an LCL-S compensation topology and W-I-shaped coupler is proposed, along with a theoretical method for calculating the coupling coefficient. Experiments show a maximum DC–DC efficiency of 94.73% at 3.1 kW input, among the highest reported for railway WPT, while maintaining robust performance under misalignment and varying load conditions. Dynamic tests demonstrate stable power delivery up to 89% efficiency and highlight the impact of transmitter spacing on power fluctuations and track design. Through two case studies on the Belmont Trolley and a 2.4 MW BEL, the system's scalability and practical feasibility are discussed.

Future work will focus on higher-power transmitter and receiver designs, advanced magnetic materials such as magnetic concrete, and adaptive control strategies to reduce efficiency variation over long tracks. Standardized railway WPT protocols will also be developed to ensure interoperability, safety, and reliable operation.

References

[1] M. E. Akay and A. Ustaoglu, "Energetic, exergetic, and environmental evaluation of railway transportation by diesel and electric locomotives," *Environmental Progress & Sustainable Energy*, vol. 41, no. 3, p. e13804, 2022.

[2] C. T. Dick, R. D. Walthall, M. E. Iden, J. Blaze *et al.*, "Cost and benefit risk framework for modern railway electrification options," United States. Department of Transportation. Federal Railroad Administration, Tech. Rep., 2025.

[3] Railway-Technology, "Caltrain electrification project costs climb to $2.44bn," https://www.railway-technology.com/news/caltrain-electrification-project-costs/, Dec. 7, 2021, accessed: 2025-04-21.

[4] J. Marsh, "Is electrifying the freight rail network cost prohibitive?" https://www.freightwaves.com/news/is-electrifying-the-freight-rail-network-cost-prohibitive, Apr. 28, 2021, accessed: 2025-04-21.

[5] I. Ernst, "Alstom to deliver 16 electric locomotives to Romania," https://www.railway-news.com/alstom-to-deliver-16-electric-locomotives-to-romania/, 2024, accessed: 2025-04-21.

[6] E. Robinson, "Alstom delivers 300th electric locomotive to Indian railways," https://www.globalrailwayreview.com/news/142872/alstom-delivers-300th-electric-locomotive-to-indian-railways/, 2023, accessed: 2025-04-21.

[7] S. Narayan, "Siemens India inks $3.2 bn electric loco deal with railways," https://www.livemint.com/news/india/siemens-india-inks-3-2-bn-electric-loco-deal-with-railways-11673892372136.html, 2023, accessed: 2025-04-21.

[8] F. Zenith, R. Isaac, A. Hoffrichter, M. S. Thomassen, and S. Møller-Holst, "Techno-economic analysis of freight railway electrification by overhead line, hydrogen and batteries: Case studies in Norway and USA," *Proceedings of the Institution of Mechanical Engineers, Part F: Journal of Rail and Rapid Transit*, vol. 234, no. 7, pp. 791–802, 2020. [Online]. Available: https://doi.org/10.1177/0954409719867495

[9] H. Weiss, T. Winkler, and H. Ziegerhofer, "Large lithium-ion battery-powered electric vehicles — from idea to reality," in *2018 ELEKTRO*, 2018, pp. 1–5.

[10] J. Morton, "Futuristic solutions deliver benefits today," *Engineering and Mining Journal*, vol. 224, no. 12, pp. 40–47, 2023.

[11] N. D. Popovich, D. Rajagopal, E. Tasar, and A. Phadke, "Economic, environmental and grid-resilience benefits of converting diesel trains to battery-electric," *Nature Energy*, vol. 6, no. 11, pp. 1017–1025, 2021.

[12] V. Leal, J. Ribeiro, E. Coelho, and M. Freitas, "Recycling of spent lithium-ion batteries as a sustainable solution to obtain raw materials for different applications," *Journal of Energy Chemistry*, vol. 79, pp. 118–134, 2023.

[13] J. H. Kim, B.-S. Lee, J.-H. Lee, S.-H. Lee, C.-B. Park, S.-M. Jung, S.-G. Lee, K.-P. Yi, and J. Baek, "Development of 1-MW inductive power transfer system for a high-speed train," *IEEE Transactions on Industrial Electronics*, vol. 62, no. 10, pp. 6242–6250, 2015.

[14] J. Huh, S. Lee, C. Park, G.-H. Cho, and C.-T. Rim, "High performance inductive power transfer system with narrow rail width for on-line electric vehicles," in *2010 IEEE Energy Conversion Congress and Exposition*, 2010, pp. 647–651.

[15] C.-B. Park, "A study on the high-efficiency coreless-typed wireless power transfer system for railway transit," *Journal of Electrical Engineering Technology*, vol. 11, no. 5, pp. 1305–1310, 2016.

[16] K. Ukita, T. Kashiwagi, Y. Sakamoto, and T. Sasakawa, "Evaluation of a non-contact power supply system with a figure-of-eight coil for railway vehicles," in *2015 IEEE PELS Workshop on Emerging Technologies: Wireless Power (2015 WoW)*. IEEE, 2015, Conference Proceedings, pp. 1–6.

[17] F. Musavi and W. Eberle, "Overview of wireless power transfer technologies for electric vehicle battery charging," *IET Power Electronics*, vol. 7, no. 1, pp. 60–66, 2014.

[18] SAE International, *Wireless power transfer for light-duty plug-in/electric vehicles and alignment methodology*, Std. SAE Standard J2954_202 408, Aug. 2024. [Online]. Available: https://doi.org/10.4271/J2954_202408

[19] ——, *Wireless power transfer for heavy-duty electric vehicles*, Std. SAE Standard J2954/2_202 212, Dec. 2022. [Online]. Available: https://doi.org/10.4271/J2954/2_202212

[20] International Organization for Standardization (ISO), *Electrically propelled road vehicles — Functional and safety requirements for power transfer between vehicle and external electric circuit — Part 4: Magnetic field wireless power transfer*, Std. ISO 5474-4:2025, Mar. 2025. [Online]. Available: https://www.iso.org/standard/81300.html

[21] J. Huh, S. W. Lee, W. Y. Lee, G. H. Cho, and C. T. Rim, "Narrow-width inductive power transfer system for online electrical vehicles," *IEEE Transactions on Power Electronics*, vol. 26, no. 12, pp. 3666–3679, 2011.

[22] J. Shin, S. Shin, Y. Kim, S. Lee, B. Song, and G. Jung, "Optimal current control of a wireless power transfer system for high power efficiency," in *2012 Electrical Systems for Aircraft, Railway and Ship Propulsion*. IEEE, 2012, pp. 1–4.

[23] C. H. Lee, G. Jung, S. Shin, Y. Kim, B. Song, J. Shin, S. H. Chung, D. O. Kim, and J. Lee, "Design and introduction of high power transfer system for electrical vehicles," in *2013 IEEE International Conference on Intelligent Rail Transportation Proceedings*. IEEE, 2013, pp. 280–284.

[24] H. Hao, G. A. Covic, and J. T. Boys, "A parallel topology for inductive power transfer power supplies," *IEEE Transactions on Power Electronics*, vol. 29, no. 3, pp. 1140–1151, 2013.

[25] J. Shin, S. Shin, Y. Kim, S. Ahn, S. Lee, G. Jung, S.-J. Jeon, and D.-H. Cho, "Design and implementation of shaped magnetic-resonance-based wireless power transfer system for roadway-powered moving electric vehicles," *IEEE Transactions on Industrial electronics*, vol. 61, no. 3, pp. 1179–1192, 2013.

[26] S. Y. Choi, S. Y. Jeong, B. W. Gu, G. C. Lim, and C. T. Rim, "Ultraslim S-type power supply rails for roadway-powered electric vehicles," *IEEE Transactions on Power Electronics*, vol. 30, no. 11, pp. 6456–6468, 2015.

[27] Y. Li, R. Mai, T. Lin, H. Sun, and Z. He, "A novel WPT system based on dual transmitters and dual receivers for high power applications: Analysis, design and implementation," *Energies*, vol. 10, no. 2, p. 174, 2017.

[28] D. Shimode, T. Murai, and T. Sawada, "Adaptation of discrete-type cores for secondary coils of wireless power transfer system for railway," *Electrical Engineering in Japan*, vol. 201, no. 2, pp. 49–57, 2017.

[29] Y. Li, J. Hu, X. Li, R. Mai, Z. Li, M. Liu, and Z. He, "Efficiency analysis and optimization control for input-parallel output-series wireless power transfer systems," *IEEE Transactions on Power Electronics*, vol. 35, no. 1, pp. 1074–1085, 2019.

[30] Y. Geng, Z. Yang, and F. Lin, "Design and control for catenary charged light rail vehicle based on wireless power transfer and hybrid energy storage system," *IEEE Transactions on Power Electronics*, vol. 35, no. 8, pp. 7894–7903, 2020.

[31] J. Deng, Y. Zhang, S. Wang, Z. Wang, and Y. Yang, "The design and coupler optimization of a single-transmitter coupled multireceiver inductive power transfer system for maglev trains," *IEEE Transactions on Transportation Electrification*, vol. 7, no. 4, pp. 3173–3184, 2021.

[32] C. H. Lee, G. Jung, K. Al Hosani, B. Song, D.-k. Seo, and D. Cho, "Wireless power transfer system for an autonomous electric vehicle," in *2020 IEEE Wireless Power Transfer Conference (WPTC)*. IEEE, 2020, pp. 467–470.

[33] B. Song, S. Cui, Y. Li, and C. Zhu, "A narrow-rail three-phase magnetic coupler with uniform output power for EV dynamic wireless charging," *IEEE Transactions on Industrial Electronics*, vol. 68, no. 8, pp. 6456–6469, 2020.

[34] S. Liu, X. Zhao, Y. Wu, L. Zhou, Y. Li, R. Mai, and Z. He, "Efficiency improvement of dual-receiver WPT systems based on partial power processing control," *IEEE Transactions on Power Electronics*, vol. 37, no. 6, pp. 7456–7469, 2021.

[35] X. Xu, L. Wang, K. Lin, T. Zhao, S.-E. Chen, D. Cook, and D. Ward, "Design considerations of an inductive power transfer system for rail application," in *IEEE Transportation Electrification Conference*, 2021, pp. 457–461.

[36] X. Xu, "Wireless power transfer for railway applications," Ph.D. dissertation, The University of North Carolina at Charlotte, 2022.

[37] H. Yoda and K. Ukita, "Wireless power transfer system for railway vehicles with improved power density of onboard coil," *Quarterly Report of RTRI*, vol. 64, no. 1, pp. 67–72, 2023.

[38] H. Yoda, "Development of WPT systems for railway vehicles and study for low-frequency application," in *2024 IEEE Wireless Power Technology Conference and Expo (WPTCE)*. IEEE, 2024, pp. 536–541.

[39] G. Lee, M. Y. Kim, S.-G. Lee, and J. H. Kim, "Operational verification of semi-dynamic wireless power transfer in light-rail transit systems," *IEEE Transactions on Transportation Electrification*, 2024.

[40] Belmont Trolley, "Powering the trolley of the future," 2024, accessed: 2025-10-03. [Online]. Available: https://https://belmonttrolley.org/innovation//

[41] X. Sun, X. Xu, K. Lin, S.-E. Chen, and T. Zhao, "Static and dynamic analysis of wireless power transfer for battery-electric locomotives," in *2024 IEEE Transportation Electrification Conference and Expo (ITEC)*, 2024, pp. 1–6.

[42] Ferroxcube, "U100/57/25 + I100/25/25 Core Datasheet," 2016, accessed: 2025-09-28. [Online]. Available: https://www.ferroxcube.com/upload/media/product/file/Pr_ds/U100_57_25_I100_25_25.pdf

[43] W. Dehui, H. Chao, Y. Fan, and S. Qisheng, "Analytical calculations of self-and mutual inductances for rectangular coils with lateral misalignment in IPT," *IET Power Electronics*, vol. 12, no. 15, pp. 4054–4062, 2019.

[44] Z. Chen, Z. Li, Z. Lin, J. Li, and Y. Zhang, "Mutual inductance calculation of rectangular coils at arbitrary position with bilateral finite magnetic shields in wireless power transfer systems," *IEEE Transactions on Power Electronics*, 2024.

[45] C. Hoer and C. Love, "Exact inductance equations for rectangular con-ductors with applications to more compli," *Journal of Research of the National Bureau of Standards: Engineering and instrumentation. C*, vol. 69, p. 127, 1965.

[46] Wabtec Corporation. (2025) FLXdrive battery-electric locomotive technology datasheet. Accessed: 2025-09-24. [Online]. Available: https://www.wabteccorp.com/FLXdrive-Battery-Electric-Locomotive?inline

[47] G. Anderson, "BNSF battery electric locomotive demonstration project final report: BNSF zero-and near zero-emission freight facilities project (zanzeff) data acquisition support," California Air Resources Board, Tech. Rep., 2021, accessed: Sep. 25, 2025. [Online]. Available: https://ww2.arb.ca.gov/sites/default/files/2022-11/zanzeff-bnsf-belreport.pdf

[48] E. Asa and O. Onar, "High-power oak ridge converter (orc) for extreme fast charging applications," Oak Ridge National Laboratory (ORNL), Oak Ridge, TN (United States), Tech. Rep., 2024.

[49] X. Sun, K. Lin, J. Zhou, S.-E. Chen, N. Braxtan, and T. Zhao, "Optimizing magnetic block structure for enhanced coupling coefficients in wireless power transfer: A finite element analysis approach," in *2024 IEEE Transportation Electrification Conference and Expo (ITEC)*. IEEE, 2024, pp. 1–6.

[50] X. Sun, S.-E. Chen, and T. Zhao, "Comparative analysis of ferrite blocks and magnetic concrete in wireless power transfer systems," in *2025 IEEE/AIAA Transportation Electrification Conference and Electric Aircraft Technologies Symposium (ITEC+ EATS)*. IEEE, 2025, pp. 1–6.

[51] X. Sun, J. Zhou, S.-E. Chen, and T. Zhao, "Improving magnetic concrete permeability by electromagnetic pulse-enhanced anisotropy," in *IECON 2024-50th Annual Conference of the IEEE Industrial Electronics Society*. IEEE, 2024, pp. 1–4.

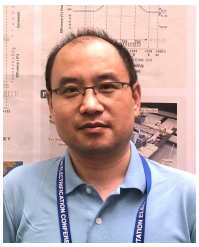

Xiuhu Sun (Graduate Student Member, IEEE) received the B.E. degree in Electrical Engineering from Shandong University, Jinan, Shandong, China, in 2002. From 2002 to 2021, he held various industry positions, including technical engineer, R&D engineer, director of the technology department, and mechanical specialist. He received his M.S. degree in Electrical Engineering from the University of North Carolina at Charlotte, Charlotte, NC, USA, in 2023, where he is currently pursuing a Ph.D. degree in Electrical Engineering. His research interests include wireless power transfer systems, DC/DC power converters, magnetic materials, and finite element analysis.

Xiwen Xu (Member, IEEE) received the B.S. degree in Electrical Engineering from Shenyang Jianzhu University and the M.S. and Ph.D. degrees in Electrical Engineering from the University of North Carolina at Charlotte. She is currently a Staff Power Electronics System Integration Engineer at Tesla, Inc., where she focuses on the design, optimization, and integration of high-performance power electronics for large-scale energy storage and charging systems. Her research interests include wireless power transfer for railway applications, energy storage system integration, solid-state circuit breaker application, and advanced power conversion technologies.

Karl Lin received the B.S. degree in Electrical Engineering and Computer Science from the National Kaohsiung University of Science and Technology, Taiwan, in 2014, and is currently a Ph.D. candidate in Infrastructure and Environmental Systems at the University of North Carolina at Charlotte, USA. His research interests include power electronics, wireless power transfer, magnetic composite materials, electric drive systems, and battery systems for transportation electrification.

Shen-En Chen, PE, received the B.S. degree in Civil Engineering, M.S. degree in Geotechnical Engineering, and Ph.D. degree in Structural Engineering from West Virginia University, Morgantown, WV, USA, in 1989, 1992, and 1996, respectively. He is currently a Professor with the Department of Civil and Environmental Engineering, the University of North Carolina at Charlotte, Charlotte, NC, USA. He has published over 78 peer-reviewed journal papers and holds four patents, including an international patent on carbon storage using concrete material. His research interests include carbon dioxide capture and storage, remote sensing technology, and geophysical prospecting.

Tiefu Zhao (Senior Member, IEEE) received the B.S. and M.S. degrees in Electrical Engineering from Tsinghua University, Beijing, China, in 2003 and 2005, respectively, and the Ph.D. degree in Electrical Engineering from North Carolina State University, Raleigh, NC, USA, in 2010. He is currently an Associate Professor with the Department of Electrical and Computer Engineering, the University of North Carolina at Charlotte, Charlotte, NC, USA. From 2010 to 2016, he was with Eaton Corporate Research and Technology, Milwaukee, WI, USA. Dr. Zhao has authored over 100 peer-reviewed journal and conference papers and holds 13 U.S. patents. His research interests include solid-state transformers, solid-state circuit protection, wireless power transfer, wide-bandgap power conversion, power electronics reliability, and fault detection.